15. Ľ.Smrčok, V.Jorík, E.Scholtzová, V.Milata, *Acta Crystallographica*, B**63**, (2007), 477.

16. Ľ.Smrčok, M.Brunelli, M.Boča, M.Kuchárik, *Journal of Applied Crystallography*, **41**, (2008), 634.

17. Ľ.Smrčok, B.Bitschnau. Y.Filinchuk, *Crystal Research and Technology*, **44**, (2009a), 978.

18. Ľ.Smrčok, M.Kuchárik, M.Tovar, I.Žižak, *Crystal Research and Technology*, **44**, (2009b), 834.

19. Ľ.Smrčok, R.Černý, M.Boča, I.Macková. B.Kubíková, *Acta Crystallographica*, C**66**, (2010), I16.

20. A.LeBail, Ľ.Smrčok, *Powder Diffraction*, **23**, (2011), 292.

21. M.Oszajca, Ľ.Smrčok, H.Pálková, W. Łasocha, *Journal of Molecular Structure*, **1021**, (2012), 70.

22. M.Šimúneková, P.Schwendt, J.Chrappová, Ľ.Smrčok, R.Černý, W.Van Beek, *Central European Journal of Chemistry*, **11**, (2013), 1352.

23. Ľ.Smrčok, P.Mach, A.LeBail, *Acta Crystallographica*,B**69**, (2013), doi:10.1107/S2052519213013365.

24. M.J.Gillan, *Contemporary Physics*, **38**, (1997), 115.

25. J.Hafner, *Acta Materialia*, **48**, (2000), 71.

L27

EXTENDING THE SAXS CAPABILITIES OF THE MULTI-PURPOSE EMPYREAN X-RAY DIFFRACTION PLATFORM

Stjepan Prugovečki, Jan Gertenbach and Joerg Bolze

PANalytical B.V., Almelo, The Netherlands

Ever increasing demands are being made of standard X-ray diffraction platforms for the analysis of materials, particularly those that are not suitable for analysis by traditional Bragg diffraction. However with increased detector size and sensitivity and improved other components the capabilities of the Empyrean multi-purpose diffraction system has been extended to allow scattering measurements. The new ScatterX78 SAXS/WAXS sample platform was recently added to the Empyrean diffraction system, enabling fast SAXS and WAXS measurements of highly diluted samples as well as measurements of weekly scattering materials under the vacuum. Combined with PIXcel3D 2x2 detector, the Empyrean system allows rapid collection of high quality 2D SAXS data. The data collected from various materials will be shown and discussed.

Session VI, Thursday, September 12

L28

CRYSTALLOGRAPHIC STUDY OF THE TERNARY SYSTEM PD-AG-TE

F. Laufek[1], A. Vymazalová[1], M. Drábek[1], J. Drahokoupil[2], M. Dušek[2]

[1]Czech Geological Survey, Geologická 6, 152 00 Praha 5, Czech Republic
[2]Institute of Physics of the AS CR, v.v.i., Na Slovance 2, 182 21, Praha 8, Czech Republic
frantisek.laufek@geology.cz

During the experimental study of phase relations on the Pd-Ag-Te system, the synthetic analogues of the mineral sopcheite $Ag_4Pd_3Te_4$ and a new phase $Ag_2Pd_{14}Te_9$ (also termed as Pd_6AgTe_4) were synthesised and structurally characterized. The mineral sopcheite was found in the Cu-Ni sulphide ores of the Sopcha massif, Kola peninsula, Russia by [1], where it occurs as veins with size not exceeding of 0.02 mm included in chalcopyrite. The $Ag_2Pd_{14}Te_9$ phase was described as small anhedral grains (<0.1 mm) by [2] from the Nadezhda deposit in Karelia, Russia. In order to understand the behaviour of these phases in the natural conditions and to clarify mechanisms of various chemical substitutions, the crystal structures of both phases have been determined.

Because of extremely low amount of natural samples and difficulties connected with their isolation, both phases were synthesized from elements by conventional solid-state reactions. Stoichiometric amounts of individual elements were sealed in silica glass tubes and resultant mixtures were heated at 350°C. After long-term annealing, the samples were quenched in a cold-water bath. The crystal structure of synthetic analogue of sopcheite $Ag_4Pd_3Te_4$ was solved from single-crystal X-ray diffraction data, whereas structure of $Ag_2Pd_{14}Te_9$ was solved from powder X-ray diffraction data.

$Ag_4Pd_3Te_4$: Space group *Cmca*, $a = 12.22$ Å, $b = 6.14$ Å, c = 12.23 Å, $V = 918$ Å^3 and $Z = 4$. In the layered structure of $Ag_4Pd_3Te_4$, the Pd atoms show a square planar coordination by the four Te atoms. The [$PdTe_4$] squares share two opposite Te-Te edges with adjacent [$PdTe_4$] squares forming layers parallel to (100). In addition, each Pd atom has four short contacts with the Ag atoms. The layers of

edge-sharing [PdTe$_4$] squares are connected by number of Ag-Te bonds running approximately in [100] direction.

Ag$_2$Pd$_{14}$Te$_9$: Space group $I4/m$, $a = 8.96$ Å, $c = 11.82$ Å, $V = 949$ A^3 and $Z = 2$. The three-dimensional framework structure of Ag$_2$Pd$_{14}$Te$_9$ consists of [PdTe$_4$] squares and [(Pd/Ag)Te$_4$] flattened tetrahedra. The squares and tetrahedra form slabs parallel to (001), which regularly alternate along the **c**-axis. The flattened tetrahedra are hallmark of this unique structure.

1. D. A. Orsoev, S. A. Rezhenova, A. N. Bogdanova, *Zap. Vses. Mineralog. Obshch*., **111**, 114, 1982.

2. A. Y. Barkov, R. F,. Martin, M. Tarkian, G. Poirier, Y. Thibault, *Can. Mineral*., **39**, 639, 2001.
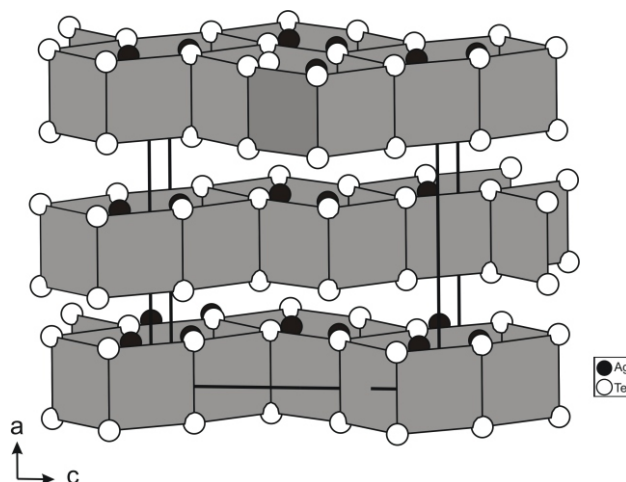
Figure 1. The crystal structure of the synthetic analogue of sopcheite Ag$_4$Pd$_3$Te$_4$ in a polyhedral representation. The [PdTe$_4$] squares are emphasised; unit cell edges are highlighted. Note the layered character of the structure.

L29

CRYSTAL STRUCTURE OF K$_2$HPO$_4$ .3H$_2$O FROM LABORATORY POWDER DATA

J. Maixner, V. Novotný

Central laboratories, Institute of Chemical Technology, Technická 5, 166 28 Prague 6, Czech Republic
maixnerj@vscht.cz

The Potassium Hydrogen Phosphate Trihydrate (K$_2$HPO$_4$ .3 H$_2$O) has got its entry in the PDF4+[1] - Card No. 00-025-0640 (Technisch Physische Dienst, Delft, Netherlands, *ICDD Grant-in-Aid)*, but its crystal structure has not been determined yet. X-ray powder diffraction data, unit-cell parameters, space group and crystal structure for K$_2$HPO$_4$ .3 H$_2$O will be reported [$a = 7.7882(7)$ Å, $b = 13.838(1)$ Å, $c = 13.833(2)$ Å, unit-cell volume $V = 1491$ Å^3, $Z = 8$, orthorhombic system, space group Pbca]. The experimental powder diffraction pattern was indexed by DICVOL04[2], solved in direct space by DASH[3] and refined in HIGHSCORE PLUS 3.0e [4]. The results of X-ray powder diffraction structure determination will be presented.

1. ICDD,"Powder Diffraction File," edited by Frank McClune, International Centre for Diffraction Data, 12 Campus Boulevard, Newton Square, Pennsylvania 19073-3272, 2012.

2. A.Boultif & D.Louër. J.Appl. Crystallogr. 37, (2004) 724–731.

3. W. I. F.David, K.Shankland, J. van de Streek, E. Pidcock, W. D. S. Motherwell, J. C. Cole. J. Appl. Cryst., **39**, (2006), 910-915.

4. HighScore Plus , Full Powder Pattern Analysis Software, V3.0e, PANalytical, Almelo, Holland .

L30

EXPLOITATION OF X-RAY DIFFRACTION IN CHARACTERISATION OF C45 FERRITIC-PEARLITIC STEEL PROPERTIES

D. Šimek[1], A. Oswald[2], R. Schmidtchen[2], M. Motylenko[1], D. Rafaja[1], G. Lehmann[2]

[1]*Institute of Materials Science, TU-Freiberg, Gustav-Zeuner-Str. 5, D-09599 Freiberg, Germany*
[2]*Institute of Metal Forming, TU-Freiberg, Bernhard von Cotta Str. 4, D-09599 Freiberg, Germany*
e-mail: simek@fzu.cz

Ferritic-pearlitic (F-P) steel C45 containing 0.45 wt.% of carbon exhibits a variable microstructure according to its thermo-mechanical treatment. After forming in austenite state, if the cooling below approx. 850 °C is slow enough, the ferritic-pearlitic microstructure develops. The primary ferrite crystallizes at the austenitic grain boundaries above the eutectoid temperature of 727 °C, below which the rest austenite is transformed into lamellar pearlite. The relative amount of primary ferrite (X_f) depends on the cooling rate, the prior austenite grain size (the smaller the grains the larger the grain boundary crystallisation area) and the upper limit is approx. 60%. The faster the cooling, the less primary ferrite is developed in favour of pearlite.

The correlation of mechanical properties of F-P steels wit their microstructure were thoroughly studied [1,2,3] as the key factors affecting the strength of pearlite, its interlamellar distance (ILD, S) was identified [1,2]. In F-P steels, the volume fraction of pearlite ($X_p = 1 - X_f$) play also an important role, but the correlation of yield strength with these two parameters is not clear [3].

The intention of study was to investigate the exposure of the microstructure in the X-ray diffraction (XRD) and the correlation of XRD features with mechanical properties of C45 F-P steel directly. The aim of the survey was to develop a fast analytical method for an on-line control of manufacturing process optimisation. In order to cope with the problem, a series of F-P microstructures was produced by hot rolling at various temperatures and by different regimes of cooling (ambient air, lead bath of 550 °C, dipping

in water). Subsequent heating was optionally also applied. Further, selected F-P microstructures representing the broad range of hot rolled F-P steels were subjected to gradual cold drawing with or without intermediate reheating. This process represented the industrial treatment from ingots till cold-drawn hard wires.

The investigation of the hot rolled samples revealed that the ferrite phase is under an apparent compressive residual stress regardless of the cut of the specimen surface (cross-sectional or longitudinal). This behaviour excludes the macroscopic residual stress. It is a consequence of two-component microstructure (ferrite/pearlite). The TEM investigation revealed the misfit dislocations at the ferrite cementite interfaces in the pearlite, while the primary ferrite grains were almost defect-free. The 3rd kind dislocation induced mean squared microstrain (ε^2_{disl}) obtained from XRD was found to correlate with the over-all density of cementite lamellas calculated as X_p/S (Figure 1). The same tendency is held also for fully pearlitic samples of steel C80D (0.80 wt.% carbon). The dependence is rather quadratic instead of linear as supposed in e.g. [4]. It is the nature of the misfit dislocations that are not randomly distributed but organized in an equidistant grid, so that their displacement fields are more similar to dislocation dipoles. The ultimate tensile strength was found to be directly proportional to the mean squared microstrain in hot-rolled samples (Figure 2).

With cold drawing, for cross-sectional reduction till about 50%, the dislocation density increases and the correlation of UTS with the mean squared microstrain can still
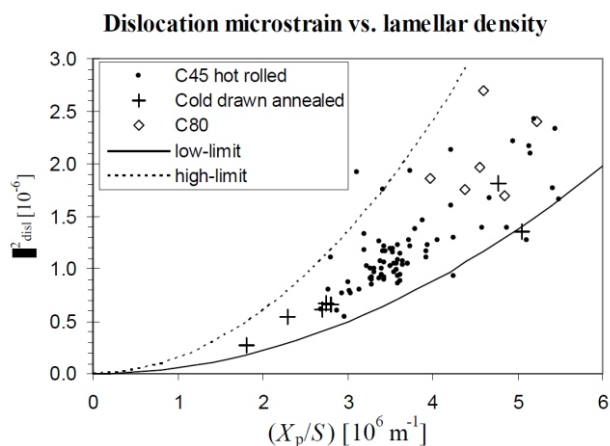
Figure 1. Correlation of dislocation-induced microstrain and over-all lamellar density in hot rolled ferritic-pearlitic C45 samples and in fully pearlitic (C80) samples. The cold drawn and subsequently annealed C45 samples are also included.
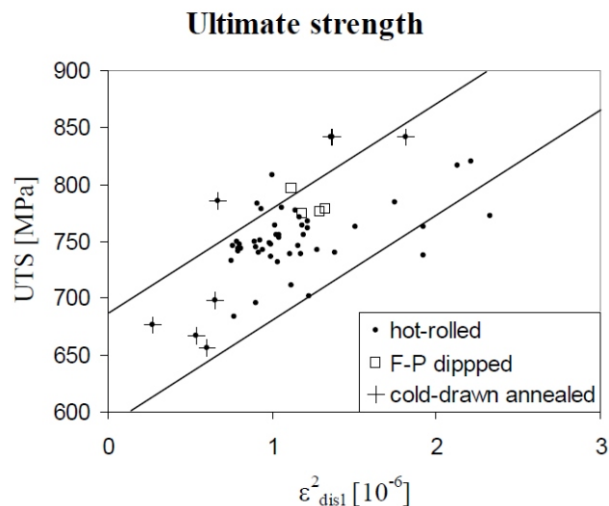
Figure 2. Correlation of UTS with mean squared dislocation induced microstrain.
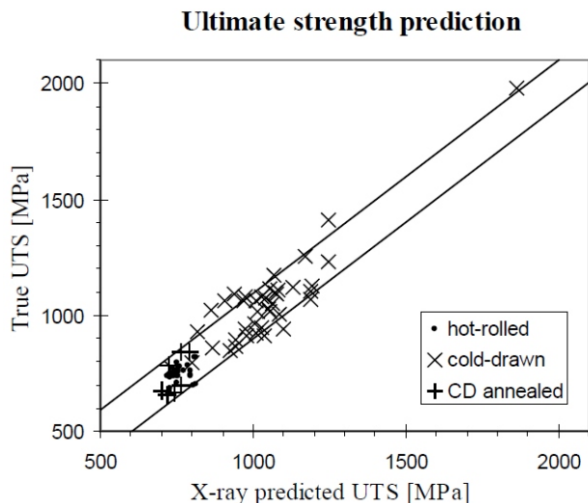
Figure 3. Comparison of UTS predicted from the X-ray diffraction experiment and true UTS evaluated in the tensile test

force), the higher is the UTS of the steel in the tensile test. The XRD here allows to determine which mechanism is driving the tensile properties. Thus, a single measurement in rolling/drawing direction is suitable for estimation of the UTS. If the a_{111} is larger than the stress-free lattice parameter, the sample is hot rolled or annealed and UTS depends on the dislocation density (analysed from the line broadening). If a_{111} is smaller, the UTS is dependent upon this lattice parameter. The XRD-predicted UTS than gives a good agreement with the true experimental UTS evaluated from the tensile test (Figure 3).

The XRD is able to predict the ultimate tensile strength of ferritic-pearlitic steel produced by the hot rolling or cold drawing in a broad range of its experimental values (600 – 2000 MPa) with the error band of approx. ± 100 MPa (cf. Figure 3). It appears therefore as a promising analytical method for a fast on-line control of the steel production. The correlation with the microstructure moreover allows to estimate the mesoscopic microstructure parameter (pearlite volume fraction or its interlamellar distance) if additional information about the thermo-mechanical history is known.

be observed, however, with a certain offset in the microstrain compared to hot rolled samples. Afterwards, for higher deformation or after annealing, the proportionality is lost. On the other hand, macroscopic residual stress is now observed in the ferrite phase, which is compressive along drawing direction. It is the result of the easier plastic deformation of the ferrite compared to harder cementite, which, after relief of the drawing force, compresses the ferrite.

A new empirical correlation was found between the UTS and the (extrapolated) lattice parameter observed on crystallographic direction 111 in the drawing direction (a_{111}). The smaller is the a_{111} (the stronger the compressive

1.   O. P. Modi, N. Deshmukh, D. P. Mondal, A. K. Jha, A. H. Yegneswaran, H. K. Khaira, *Materials Characterization* **46**, (2001), pp. 347-352.

2.   A. M. Elwazri, P. Wanjara, S. Yue, *Mat. Sci. Eng. A* **404**, (2005), pp. 91-98.

3.   K. K. Ray, D. Mondal, *Acta Metall. Mater.* **39**, (1991), pp. 2201-2208.

4.   T. Ungár, I. Dragomir, Á Révész, A. Borbély, *J. Appl. Cryst.* **32**, (1999), pp. 992-1002.

L31

TOWARD THE FINAL EXPLANATION OF MARTENSITIC TRANSFORMATION IN SHAPE MEMORY ALLOY CO-NI-AL

J. Kopeček[1], M. Jarošová[2], K. Jurek[2], J. Drahokoupil[1], I. Kratochvílová[1], L. Fekete[1], L. Bodnárová[3], H. Seiner[3], P. Sedlák[3], M. Landa[3], J. Šepitka[4], J. Lukeš[4], V. Kopecký[1], O. Heczko[1]

[1] *Institute of Physics of the AS CR, Na Slovance 2, 182 21 Praha 8, Czech Republic*
[2] *Institute of Physics of the AS CR, Cukrovarnická 10/112, 162 00 Praha 6, Czech Republic*
[3] *Institute of Thermomechanics of AS CR, Dolejškova 5, 182 00 Prague 8, Czech Republic*
[4] *Laboratory of Biomechanics, CTU in Prague, Technická 4, 166 07, Prague 6, Czech Republic*
kopecek@fzu.cz

Great success in Ni_2MnGa derived alloys [1,2] attracted attention to similar Heusler alloys including cobalt based CoNiAl and CoNiGa [3,4]. As the NiMnGa alloys suffer due to their strongly intermetallic state (brittleness, poor creep and fatigue properties) the cobalt based alloys seemed to be the interesting candidate for the mechanically stronger and more resistant FSMAs.

The article describes the progress in work on $Co_{38}Ni_{33}Al_{29}$ alloy [5,6]. The defined crystals with single-crystalline matrix were prepared after long struggling. The influence of annealing on martensitic transformation

was investigated. Both post-mortem XRD and in-situ neuron diffraction confirmed the martensitic phase transformation of alloy matrix B2 $\rightarrow$ $L1_0$ and stable amount of A1 particles (fcc cobalt solid solution) in alloy, Fig. 1. The image of transformation paths is blurred considering the results of resonant ultrasound spectroscopy (RUS), magnetic susceptibility measurements and various microscopies (LOM, SEM, AFM), which shows transformation temperature significantly higher (about approx. 70 °C). Without regard to structural confusion all samples perform
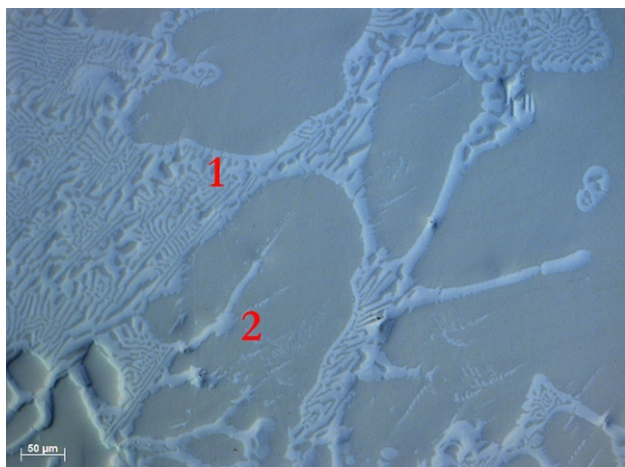
Figure 1. The structure of the samples observed by scanning electron microscopy. The precipitates marked 1 are interdendritic A1 fcc cobalt solid solution particles. The precipitates marked 2 are $L1_2$ ordered precipitates of the phase $(Co,Ni)_3Al$.

pseudoelastic behaviour at room temperature, which is strongly dependent on crystallographic orientation.

Nevertheless, the role of nanoprecipitates resulting from segregation in oversaturated matrix after annealing or other changes in matrix induced by quenching seems to be indisputable [7]. These precipitates can serve as nucleation centres for the stress induced martensitic transformation. Nanoprecipitates were observed in annealed samples but in both pseudoelastic [8] and non-pseudoelastic samples [9]. The wide variety of nanoprecipitates is described in Ref. [4], nevertheless their necessity for pseudoelastic behaviour was not proven. The many micron-sized non-twinned, single and triple $\{111\}_p$ twinned precipitates with partial $L1_2$ ordering were observed in the austenite matrix after annealing at 1373 K for 72 h and quenching [10]. The final description of A1 interdendritic particles dissolution and the role of precipitation after quenching is still under the process.

The more optimistic view we have now on various results of "transformation" given by different methods. The strong magnetoelastic coupling can be documented by the evolution of damping in RUS [11]. Surprisingly the effect of magnetic field in Co-Ni-Al austenite, considering the external field, is very weak [12]. We can expect now that the finalization of the oriented cuboid samples will give us the full elastic constants set in temperature dependence and the story of "martensitic transformation" in Co-Ni-Al alloys would be finally explained.

1. Heczko O., Scheerbaum N., Gutfleisch O., *Magnetic Shape Memory Phenomena*, in *Nanoscale Magnetic Materials and Applications*, edited by J.P. Liu et al. (Springer Science+Business Media, LLC), 2009, pp. 14-1.

2. Heczko O, Sozinov A, Ullakko K, IEEE Trans. Magn., **36**, (2000), 3266-3268.

3. K. Oikawa, L. Wulff, T. Iijima, F. Gejima, T. Ohmori, A. Fujita, K. Fukamichi, R. Kainuma, K. Ishida, *Appl. Phys. Lett.*, **79**, (2001), 3290.

4. Yu. I. Chumlyakov, I. V. Kireeva, E. Yu. Panchenko, E. E. Timofeeva, Z. V. Pobedennaya, S. V. Chusov, I. Karaman, H. Maier, E. Cesari and V. A. Kirillov, *Russ. Phys. J.,* **51**, (2008), 1016.

5. J. Kopeček, S. Sedláková-Ignácová, K. Jurek, M. Jarošová, J. Drahokoupil, P. Šittner, V. Novák: *Structure development in $Co_{38}Ni_{33}Al_{29}$ ferromagnetic shape memory alloy*, 8th th European Symposium on Martensitic Transformations, ESOMAT 2009, edited by Petr Šittner, Václav Paidar, Luděk Heller, Hanuš Seiner, 2009, article No. 02013.

6. J. Kopeček, K. Jurek, M. Jarošová, et al., *IOP Conf. Sci.: Mater. Sci. Eng.*, **7**, (2010), 012013.

7. J. Kopeček, V. Kopecký, M. Landa, O. Heczko, Mat. Sci. Forum, 738-739, 416-420, (2013)

8. B. Bártová, N. Wiese, D. Schryvers, N. J. Chapman, S. Ignácová, Acta Mater., 56 (2008), 4470-4476.

9. B. Bártová, D. Schryvers, Z. Q. Yang, S. Ignácová, P. Sittner, Scripta Mater., 57 (2007), 37- 40.

10. J.B. Lu, H. Shi, S. Sedláková-Ignácová, R. Espinoza, J. Kopeček, P. Šittner, B. Bártová, D. Schryvers, J. Alloys Comp., 572, 5-10, (2013).

11. H. Seiner, J. Kopeček, P. Sedlák, L. Bodnárová, M. Landa, P. Sedmák, O. Heczko, Acta Mater., 61, 5869-5876, (2013).

12. O. Heczko, H. Seiner, P. Sedlák, J. Kopeček, V. Kopecký, M. Landa, Eur. Phys. J. B, 86:(2), 62-1 – 62-5, (2013).

L32

STRUCTURE, MICROSTRUCTURE AND RESIDUAL STRESSES IN BORIDED STEELS

Z. Pala[1], R. Mušálek[2], J. Kyncl[3], P. Harcuba[4], J. Stráský[4] , K. Kolařík[1]

[1]*Department of Solid State Engineering, Faculty of Nuclear Sciences and Physical Engineering, Czech Technical University in Prague, Trojanova 13, Prague, Czech Republic*
[2]*Department of Materials Engineering, Institute of Plasma Physics, Za Slovankou 1782/3, Prague, Czech Republic*
[3]*Department of machining, process planning and metrology, Faculty of Mechanical Engineering, Czech Technical University in Prague, Technická 4, Prague, Czech Republic*
[4]*Department of Physics of Materials, Faculty of Mathematics and Physics, Charles University in Prague, Ke Karlovu 5, Prague, Czech Republic*
*zdenek.pala@fjfi.cvut.cz*

Boriding or boronizing belongs to thermo-chemical diffusion-based surface hardening of iron materials. Even though it is comparatively rarely applied in industrial processes in comparison with other treatments, it can lead to substantial increase of service life, especially when extreme wear occurs on the surface. The main virtues of borided surface are not only the high hardness surpassing in some cases even 2000 HVN (Vickers hardness number), but also very low friction coefficient and above-average resistance to an array of acids and to high-temperature oxidation in a broad range of temperatures from ambient up to approximately 1000 °C. For example, the intrinsic hardness of Fe_2B is 1700 HVN or by order of magnitude higher than of pure iron with 130 HVN [1]. In general, whereas boriding leads to 1500 to 2000 HVN, the most widely applied treatments of nitriding and carburizing lead to 600 ÷ 1100 HVN and 700 ÷ 850 HVN, respectively [2]. At the same time, borided layers exhibit high thermal and electrical conductivity which can be an asset when compared with e.g. ceramic wear protective layers. Probably the main advantage of the borided process is such that it imposes virtually no limitations of the shape of the borided object, since the boron sublimates at higher temperatures from the boron source (typically powder) adjacent to the borided surface and penetrates into it via diffusion mechanism.

Both the boriding process and the structure of the resulting zone consisting of borided layers, base material and the interface in between them are intriguing since the complete description of the boriding mechanism is still lacking. Moreover, the structural phenomena involved encompass not only two distinct crystalline phases of tetragonal Fe_2B, which has three polymorphs with space groups I-4/mcm or $I\bar{4}2m$, and orthorhombic FeB (Pbnm), but also substantial residual stresses differing both in values and even character in both phases and with appreciable stress gradient, texture is often present and also grain boundaries represent a fairly complex structural issue. From the microstructural point of view, the interface between the borided layers and base material is commonly described as having "tooth-shaped" or "saw-tooth" character as seen in Fig. 1. The spatial layout of the phases is usually such that FeB is on the surface and the needles in deeper layers are grains of Fe_2B. Consequently Fe_2B layers tend to exhibit higher degree of preferred orientation, most commonly fibre texture [3], yet texture of FeB layers is no exception. Since FeB is the
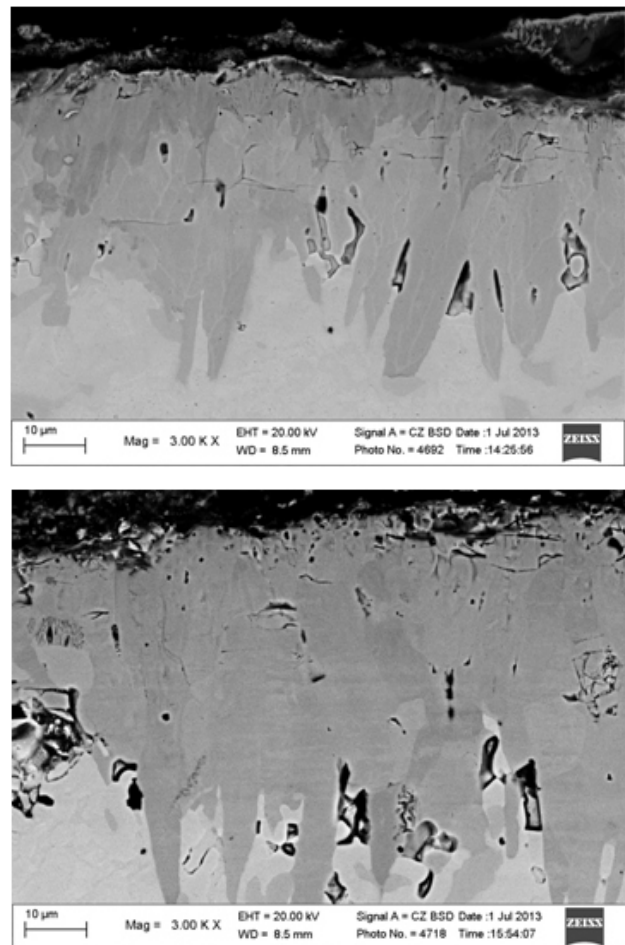
Figure 1. "Tooth-shaped" microstructure of borided layers created in the surface of hard-to-work chromium ledeburitic steel X210Cr12 after 5 hours (upper) and 12 hours (lower) of boriding at 930 °C in powder.

brittler phase, the single phase borided layer of Fe_2B with good toughness is usually preferred to the duplex phase Fe_2B + FeB layer. Moreover, since the FeB is distinguished by almost triple value of thermal expansion coefficient when compared with the base material, it usually decomposes from the borided object during cooling after the boriding process, which is described as thermo-mechanical spalling.
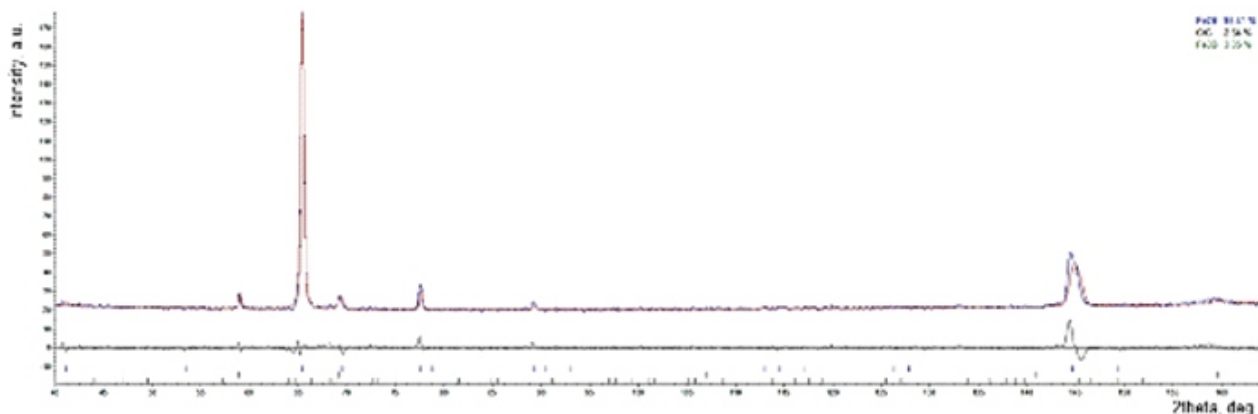
Figure 2. Result of Rietveld refinement showing dominant presence of Fe_2B, in order to take texture into account, March-Dollase metod was employed. The macroscopic residual stresses were not considered, hence the shift of modelled date at higher 2 at 145°.

In general, there are two parameters of borided surface which are being optimized via the boriding process conditions. Firstly, the effort is aimed at obtaining such microstructural morphology that would lead to better toughness and ductility coupled with sufficient adhesion of the borided layers facilitated by the tooth-shaped interface. Secondly, the spatial distribution of macroscopic residual stresses in the borided layers and the adjacent area of substrate should be such that would favour good cohesion within the hard layers and also contribute to the adhesion of the surface to the bulk.

The existence of texture significantly hinders the calculation of residual stresses in iron borides, especially in Fe_2B. So far, the texture was omitted in the calculation of residual stresses and we are currently developing an algorithm to take the effect of texture into account. In order to do this, single crystal elastic constants have to be known. There have been several attempts to calculate them using DFT (Density functional theory), but the results differ by as much as 100 %. Hence, residual stresses are calculated with macroscopic, or bulk, elastic constants in the generalized Hooke equation which can bring about unreliable results.

The aim of the hitherto carried out analyses was to ascertain whether boriding can bring beneficial effects to

highly alloyed hard-to-work chromium ledeburitic steel X210Cr12 suitable for cold forming tools. The high levels of carbon (1.9 ÷ 2.2 wt%), silicon (0.1 ÷ 0.6 wt%) and especially chromium (11 ÷ 13 wt%) have so far rendered the boriding infeasible. This material is a standard for silica and alumina pressing tools or moulds which also explains the practical necessity to improve its wear resistance. Pursuing this aim, the real parts of pressing mould were borided for 5 and 12 hours, respectively. The resulting objects with borided surfaces were examined by SEM (Scanning electron microscopy), phase composition and residual stresses were determined from X-ray diffraction and microhardness was measured on the cross-section of the samples by Vickers indentor.

Micrographs from SEM revealed than the prolongation of processing time had only marginal effect on the borided layer thickness, increasing from approximately 30 to 40 m. However, the important difference between both microstructures (see Fig. 1) is the change from duplex to almost single phase. This was verified by X-ray diffraction (CrK radiation) when the diffraction patterns were obtained on the original free-surfaces and in depths of 10 and 20 m. Phase identification revealed presence of both Fe_2B and FeB on the surface of 5h borided sample, but only FeB on 12h borided one. Both surfaces included also phases of iron borate Fe_3BO_5. After electro-chemical removal of 20 m thick surface layer, only Fe_2B was found in both samples; the 12h sample included also minor phase of CrC and Fe_3B while the 5h sample contained CrC, Cr_7C_3 and $Fe_{23}(C,B)_6$. Rietveld refinement of the 12h sample showed about 93 wt.% of Fe_2B as seen in Fig. 2, the comparatively bad match between the measured and modelled data at 145 °2 is clear evidence of macroscopic residual stress presence which were not considered in this refinement. The most pronounced diffraction peak in Fig. 2 is from CrK diffraction on textured (002) planes of Fe_2B and were the irradiated volume without preferred orientation this peak would have 25% relative intensity of (211) peak at approximately 70 °2.

Mutual comparison of diffraction patterns obtained at the surface of both samples is in Fig. 3. Measured values of microhardness in the borided layers were surprisingly
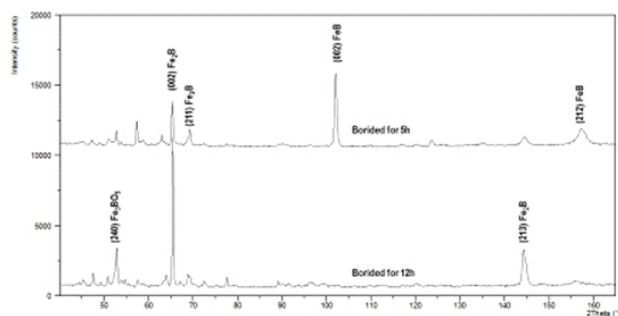
Figure 3. Comparison of diffraction patterns obtained on the surfaces of both samples.
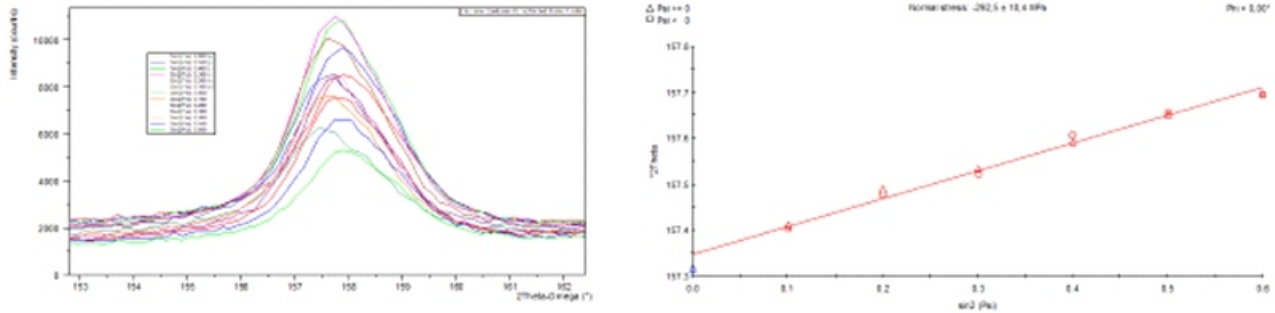
Figure 4. Measured diffraction profile of (212) planes of FeB (left) and 2θ vs. $\sin^2\psi$ dependence from which the value of macroscopic residual stress was calculated.

small, i.e. 1350 ± 180 HVN and 1520 ± 220 HVN for 5h and 12h samples, respectively. The correct calculation of residual stresses was possible only for FeB, where (212) planes were measured in various orientations to the surface taking advantage of the so-called omega geometry. The resulting dependence of inteplanar lattice spacing versus $\sin^2\psi$ was linear and the calculated value of macroscopic residual stress was approximately -300 MPa as seen in Fig. 4.

1. C.T.Zhou, J.D. Xing, B.Xiao, *Comp. Mat. Sci.*, **44**, (2009), 1056-1064.

2. P. Gopalakrishnan, P. Shankar, M. Palaniappa, *Met. and Mat. Trans. A,* **33**, (2002), 1475-1485.

3. R. Prűmmer, W. Pfeiffer, *J. Less-Common Met.*, **117**, (1986), 411-414.